Study of the Polarization Behavior of Ce0.9Gd0.1O2- Single Crystals below 350°C to Room Temperature

Neuhaus, K.; Bernemann, M.; Hansen, Karin Vels; Jacobsen, Torben; Ulbrich, G.; Heppke, E. M.; Paun, M.; Lerch, M.; Wiemhöfer, H.-D.

Published in:
Electrochemical Society. Journal

Link to article, DOI:
10.1149/2.1101614jes

Publication date:
2016

Document Version
Peer reviewed version

Study of the polarization behavior of $Ce_{0.9}Gd_{0.1}O_{2-\delta}$ single crystals below 350 °C to room temperature

K. Neuhaus°, M. Bernemann°, K. Vels Hansen[#], T. Jacobsen* , G. Ulbrich[§], E. M. Heppke[§], M. Paun[§], M. Lerch[§], H.-D. Wiemhöfer°

° University of Münster, Institute for Inorganic and Analytical Chemistry, Corrensstr. 28/30, D-48149 Münster, Germany [#] Department of Energy Conversion and Storage, Technical University of Denmark, Frederiksborgvej 399, DK-4000 Roskilde, Denmark, * Department of Chemistry, Technical University of Denmark, Kemitorvet, Building 206, DK-2800 Kgs. Lyngby, Denmark [§] Technische Universität Berlin, Institute for Chemistry, Straße des 17. Juni 115, D-10623 Berlin, Germany

Abstract

Single crystalline ceria samples with the composition $Ce_{0.9}Gd_{0.1}O_{2-\delta}$ were pre-polarized with ±5 V for up to 300 s using a Pt coated AFM tip as working electrode. The direct contact zone had a diameter of < 50 nm. Subsequently, the effect of the polarization on the surface potential of the samples was investigated by mapping the introduced defect gradient and its decay with time using Kelvin probe force microscopy. The generated surface potential gradients were found to have a diameter of up to 1 µm, which is explained by the local ionization of defect associates by the applied high electric field. Measurements were performed at room temperature and 50 °C. The polarization behavior of the $Ce_{0.9}Gd_{0.1}O_{2-\delta}$ single crystals was compared to cyclovoltammetry and polarization-relaxation experiments at T ≤ 350°C and in dry air or nitrogen which were performed using a specially suited AFM (Controlled Atmosphere High Temperature Scanning Probe Microscope CAHT-SPM by Semilab).

1 Introduction

Variably doped CeO_2 is already widely used as an electrolyte in solid oxide fuel cells or for gas sensor materials in the temperature range between 400-800 °C [1-6]. Nevertheless, chemical reactions of doped ceria in the low temperature range between room temperature and 300 °C are of increasing interest especially for novel catalytic applications [7-9]. Even at room temperature, ceria still shows a considerable oxygen buffering capacity, which cannot simply be explained by extrapolation from high temperature results [10, 11]. Systematic electrochemical investigations in the low temperature range and with microscopic resolution will be necessary to fully understand the interplay between surface and bulk reactions and to develop comprehensive theoretical models to explain the low temperature electrochemical behavior.

The high oxygen storage capacity of acceptor doped ceria occurs due to the possibility of a high oxygen vacancy ($V_O^{\circ\circ}$) concentration in the structure. Depending on the nature and amount of the dopant, ceria can therefore exclude or include oxygen and thus it is able to control the partial pressure conditions for a variety of chemical processes and this feature is already widely used for catalytic applications. At least at high temperatures, oxygen is incorporated on oxygen vacancies in the structure [12, 13]:

$$\frac{1}{2}O_2 + V_O^{\circ\circ} + 2e' \rightleftharpoons O_O^x. \quad \text{(eq. 1)}$$

At lower temperatures, the concentration of defect associates in ceria is thought to increase significantly due to trapping of electrons, allowing also for singly charged (V_O°) or uncharged (V_O) oxygen vacancies in close vicinity to Ce^{3+} ions [14-16]. The increase of partly ionized oxygen vacancies changes the electrochemical behavior at low temperatures dramatically. For low temperatures, the common electroneutrality equation for acceptor doped ceria can be extended to [16], where oxygen on interstitial lattice sites is negligible at or below atmospheric oxygen partial pressure:

$$0 = [h^{\circ}] + 2[V_O^{\circ\circ}] + [V_O^{\circ}] - [e'] - 2[O_i''] - [O_i'] - [M_{Ce}'] \quad \text{(eq. 2)}$$

$$\Rightarrow [h^{\circ}] + 2[V_O^{\circ\circ}] + [V_O^{\circ}] \approx [e'] + [M_{Ce}']$$

This study aims at gathering data on local transport processes of 10 cat% Gd doped ceria single crystals in the range from 350 °C to room temperature. So far, electrochemical measurements of high temperature mixed conductors at room temperature are extremely difficult to achieve with standard measurement techniques such as micro contact DC measurements, because the resulting currents are very low. Therefore, Kelvin probe force microscopy (KPFM) represents a possible alternative for a variety of electrochemical experiments, as described in the following sections. The results will possibly also shed light on the mobility of defects on ceria surfaces at low temperature where contradicting findings obtained by scanning probe microscopy have been published [14, 17, 18].

The composition $Ce_{0.9}Gd_{0.1}O_{2-\delta}$ (CGO) was chosen because of the high abundance of literature on the electrochemical characteristics of Gd-doped ceria materials [1, 5, 13, 19]. Hence, our results are easily comparable to “standard” electrochemical measurements.

2 Theoretical considerations

2.1 Kelvin probe force microscopy

Kelvin probe force microscopy (KPFM) is a scanning probe microscopy technique invented by Nonnenmacher et al. [20, 21]. It enables observation of the topography of a sample in combination with the surface potential at a high lateral resolution [22-25]. The KPFM technique offers a possibility to map local changes in defect concentrations [22, 26] and surface processes [27], and is therefore ideally suited to investigate the question of the contribution of surface and bulk to the redox activity of ceria. KPFM is performed in intermittent contact mode with the cantilever vibrating at its resonance frequency. During the measurement, an AC potential with a certain frequency and amplitude is applied to the AFM tip. This AC potential is fixed by an additional external voltage U_{DC} which compensates the surface potential difference between sample and probe tip [22] according to

$$U_{KPFM} = -\frac{1}{e}\Delta\varphi_{CPD} = -U_{DC} \approx \varphi \quad \text{(eq. 3)}$$

A surface plot of the potential difference -U_{DC} during the surface scan of the probe tip yields the KPFM image. The contact potential difference ($\Delta\varphi_{CPD}$) is proportional to the difference of the work functions of the platinum coated AFM tip and the sample ($\Delta\varphi_{CPD} = \Delta\phi_e$, cf. Fig. 1A).

$$\Delta\Phi_{CPD} = \Phi_{Pt} - \Phi_{CGO} \quad \text{(eq. 4)}$$

The work function is proportional to the difference in the Fermi energy levels of the tip and the sample. Therefore, changes in the defect concentration of the sample can be detected, assuming the work function of the tip is unchanged during the experiments. As the KPFM measurements were not executed in vacuum but in air, an influence of adsorbed water and other adsorbed species on the measurement signal cannot be ruled out. Water acts as a dipole which can be aligned e.g. in an electric field and which can have an additional effect on the KPFM signal. We assume the surface water layer to stay more or less constant throughout our measurements.

2.2 Defect concentrations and surface potential

When a metallic electrode (in our experimental setup the platinum coated AFM tip) is in contact with a semiconductor (the doped single crystal), an equilibrium is established, where the electrochemical potential of electrons $\tilde{\mu}_e$, which is equal to the Fermi energy E_F,

$$\tilde{\mu}_e = \mu_e + z_e F\varphi = E_F \quad \text{(eq. 5)}$$

has to be equal on both sides of the interface. This means

$$\mu_{e,Pt} - F\varphi_{Pt} = \mu_{e,CGO} - F\varphi_{CGO} \quad \text{(eq. 6)}$$

The exchange between the metal and the CGO leads to the development of a space charge region in the electrolyte, which is compensated by an increased charge concentration on the surface of the metallic electrode (see Fig. 1).

The Fermi level of the CGO is fixed in a position near the valence band by the concentration of the Gd^{3+} acceptor dopant. By applying a bias between sample and tip, charge is redistributed within the material, leading to the introduction of a defect gradient which is accompanied by a local change of the Fermi energy.

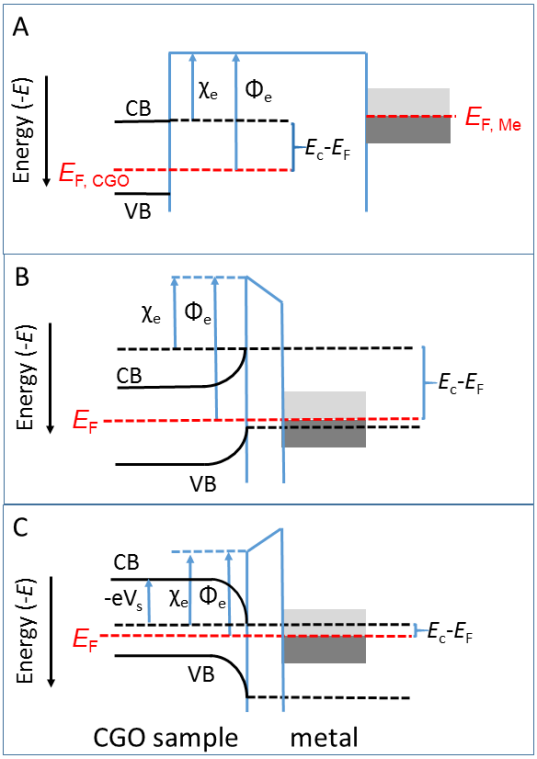

Fig. 1: Schematic band diagram of the CGO sample [28]: A) shows the initial state of the CGO sample and the metallic AFM tip without contact. The Fermi energy level of CGO is not in the middle of the band gap but near the valence band due to acceptor doping. B) and C) show the equilibrium state of the metallic tip and the CGO without direct surface contact (e.g. by wiring). The Fermi level is aligned. B) depicts the state for a metallic tip with a higher surface potential than the sample. C) depicts the state for a metallic tip with a lower surface potential than the sample. E_F = Fermi energy level, X_e = electron affinity of the sample, Φe = surface potential, –eVs = band bending.

2.3 Combining polarization and KPFM measurements

Compared to the high temperature electrochemical behavior, which is mainly described in publications, doped ceria shows a significantly distinguished behavior near room temperature, which was summarized very well by Maier et al. [15, 16, 29, 30]: The ionic conductivity at room temperature is negligible as the oxygen vacancies are in a frozen state. Mainly electrons and holes are assumed to be mobile, but the electronic conductivity of acceptor doped ceria is comparably low even at high temperature [12, 13].

A first attempt of measuring low temperature transport effects by an approach combining polarization and Kelvin probe force microscopy has already been made by this group for polycrystalline $Ce_{0.8}Gd_{0.2-x}Pr_xO_{2-\delta}$ pellets at room temperature [31] and by Lee et al. for doped ceria thin films [27]. Further, Ding et al. used external polarization of undoped ceria thin films with comparably high DC biases (about 30 V) and parallel time-dependent KPFM mapping at temperatures between 25-135 °C and at variable relative humidity to gather information on proton conductivity at triple phase boundaries.

Apart from these KPFM-related studies, Farrow et al. studied the spatial variation of conductance of a ceria thin film on the nanometer scale by AFM current-voltage mapping [32] and Yang et al. studied the effect of adsorbed water on the surface of a ceria thin film during

polarization with high positive biases (≥10 V) [33]. All studies showed a distinct polarization-relaxation behavior of the samples which depends on sample composition, grain size of the samples, temperature, applied bias and the surrounding atmosphere. In contrast to the studies mentioned above, in this work we will focus solely on a single crystalline material to monitor the effect of polarization of the bulk of ceria without interference from grain boundaries.

For the combined polarization-KPFM measurements presented here, the Pt coated AFM tip is used in two different functions: during the polarization of the sample, the tip is applied as a nanosized working electrode. Directly after the end of the polarization experiment, the KPFM mapping is started, where the tip now acts as reference for the contact potential measurements. By comparing a KPFM map of the pristine surface made before the polarization and a sequence of maps taken after the end of the polarization, a gradient of the surface potential directly after polarization and the time dependent decay of this gradient can be monitored.

The setup presented in this work was modelled with Comsol Multiphysics 4.2 (cf. Fig. 2) to predict if the effect on the surface potential should show a symmetric (circular) or asymmetric shape due to the asymmetric cell setup with small working electrode and a large silver counter electrode on one side of the sample. As a first working hypothesis, the sample in our case can be assumed to be a dielectric because of the very low charge carrier mobility at room temperature. By applying a voltage between the tip and a large back contact, the sample becomes polarized. Taking into account the conductivity and relative permittivity of the Gd-doped ceria sample it was demonstrated that due to the asymmetric cell setup a significant voltage drop during polarization occurs near the cantilever tip while the rest of the sample should not be affected strongly.

When a steady state is reached, the area of changed potential has a circular shape with a slightly flattened penetration in the z-direction in the direct vicinity of the tip (cf. Fig. 2). Comparing the diameter of the tip (about 50 nm) with the diameter of the affected area in Fig. 2, it becomes obvious, that the affected area has roughly two times the size of the tip diameter. The material in our experiments was polarized with up to ±5 V, which means, that the electric field strength in direct vicinity of the tip is very high as the electric flux lines are focused on a very small contact area. The electrical field strength we can derive from the simulation in Fig. 2 is in the area of 5 $MV \cdot m^{-1}$.

For similar KPFM-polarization experiments, Lee et al. [27] discussed the role of an adsorbed water layer on the measurements, as all our measurements are executed in ambient air and room temperature. Due to the high field strength in the direct vicinity of the tip during the polarization experiment the adsorbed water film is probably locally dissociated and does not play a role during the polarization itself. Lee et al. showed, that the surface potential of ceria also changes after polarization in a high vacuum environment or at higher temperatures, where the water layer should be negligible. Polarization in vacuum in their work had no effect on the size and intensity of the introduced gradient but the relaxation behavior was strongly affected. Hence, we can safely assume that the influence of the adsorbed water layer can be neglected during polarization in ambient conditions. In our case in first instance, the contribution of the adsorbed species was assumed to stay constant during the subsequent KPFM measurement. Humidity

from the surrounding air and unaffected areas of the sample could nevertheless be responsible for filling up part of the created oxygen vacancies as OH^- can be incorporated into oxygen vacancies and also proton conductivity can be found for polycrystalline ceria at room temperature [27, 34, 35]. This has already been demonstrated to be of considerable influence for volume expansion of ceria thin films during polarization with high positive biases (≥10 V) by AFM tip [33]. As the applied biases in our study were kept in the range of max. ±5 V, a strong reversible or irreversible change of the surface height of the CGO crystal was not expected and was not found during our study.

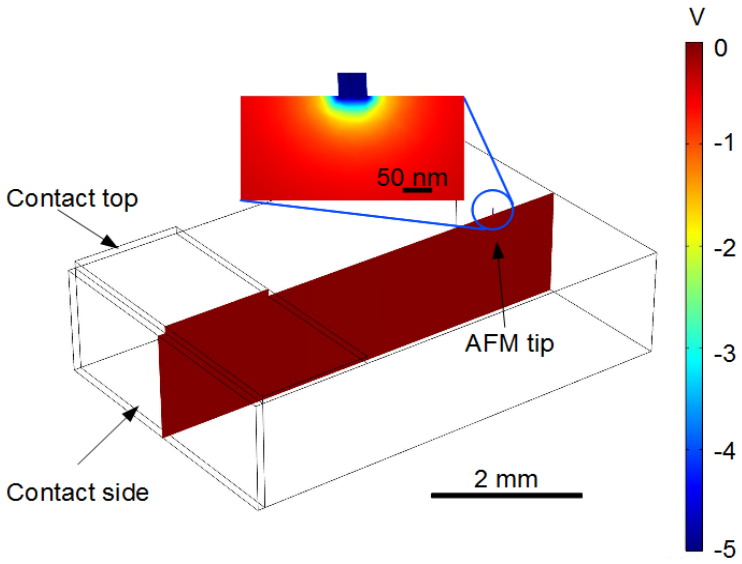

Fig. 2 Three-dimensional model of the measurement setup showing the potential distribution in the steady state with large contacts at the left side covering part of the top and the side of the sample (ground) and the AFM tip contact on the right hand. The area around the AFM tip is enlarged. The AFM tip has a diameter of about 50 nm (commercial tip) and is put in contact several mm away from the silver paste counter electrode. This electrode has a diameter of about 4 mm and is put not only on top but to some extend also on the side of the sample.

3 Experimental

3.1 Measurement method

Two different scanning probe microscopes (SPM) were used. The general measurement setup can be found in Fig. 2. Direct current single point measurements with variable atmospheres and temperatures up to 328 °C sample temperature were performed in the controlled atmosphere high temperature (CAHT-2) SPM [36] with an attached Gamry potentiostat. The oxygen partial pressure in the measurement chamber was monitored with a self-made pO_2 sensor. The surface temperature was calibrated in a separate experiment where a thermo couple was attached to the surface of the sample.

Measurements in air and at temperatures below 100 °C were conducted with an Keysight 5500 AFM with a heating sample stage using a Lakeshore 331 temperature controller. The sample

surface temperature was controlled externally with an IR thermometer. With the Keysight 5500, topography and surface potential are measured simultaneously in single pass mode. For all measurements, either home-made Pt/Ir metal probes with a diameter of roughly 1 µm (for the CAHT-2) or commercially available Pt/Ir-coated probes with a diameter of roughly 50 nm (PPP-NCSTPt by Nanosensors for the Keysight 5500) were used.

3.1.1 KPFM measurements after polarization

For monitoring the effect of the polarization on the surface potential, the AFM cantilever was used as a working electrode to polarize the surface. A Pt wire as counter electrode was fixed on one side of the sample using silver paste. This resulted in an asymmetric cell setup, with a counter electrode in the mm range and a working electrode in the nm range (cf. Fig. 2). The electrodes were placed 2-8 mm apart during polarization and subsequent measurements. The measurements were executed in air at room temperature and 50 ± 2 °C using the Keysight 5500 with attached heating sample stage.

For each experiment, an area of the sample surface was chosen and contacted with the cantilever. The area was then polarized using biases of ± 5 V for 300 s. Subsequently, the surface area was scanned again with a sampling rate of one image per minute to monitor the changes of the surface potential at the sample surface. The application of a bias has a similar effect as changing the atmosphere around the sample. A local polarization leads to a confined reduction or oxidation of the sample surface and can be associated with local effects on the surface potential. Similar effects have already been shown for polarization with oxygen conductive perovskites using electrochemical strain microscopy [37]. In contrast to these measurements, the polarization experiments presented here did not lead to a detectable change in the surface topography, which is consistent to experiments by Farrow et al. [32], who reported irreversible surface damage for polarization of ceria films with currents higher than 1 nA.

3.1.2 Single point polarization-relaxation measurements

For the single point polarization-relaxation measurements, an AFM topography image of the sample surface was obtained first. Subsequently, the cantilever was positioned on a chosen spot on the surface and polarization measurements were executed using a Gamry potentiostate, either with a fixed bias or in form of cyclic voltammetry experiments. Data were obtained at different temperatures up to 328 °C sample temperature and in dry air or N_2 atmosphere respectively.

3.2 Sample preparation

Cerium (IV) oxide (1549 g; 99.9%; Chempur) and gadolinium sesquioxide (181 g; 99.9%; Chempur) were blended in a powder mixer. Large single crystals (2x2x5 mm^3) of the resulting powder were grown using the skull melting technique [38, 39]. The melt was moved over a time of 4:20 h at a rate between 1.5 and 12 mm/h out of the hot zone. The maintained crystals were analyzed by means of X-ray diffraction (crystal structure) and electron beam microprobe (Gd/Ce concentration and homogeneity of distribution). These measurements support the

presence of homogenous fluorite-type crystals with the desired composition of $Ce_{0.9}Gd_{0.1}O_{2-\delta}$, denoted as CGO10 in this text.

The CGO10 samples were cut and polished before starting AFM investigations. As they showed a darker color due to oxygen deficiency from the skull melting procedure, they were annealed at 400 °C in air for 4 h and then slowly cooled down to room temperature to reach equilibrium with ambient oxygen partial pressure. Single crystals had a size between 2-6 mm and a thickness of about 1.5 mm.

4. Results and Discussion

4.1 Single point measurements

Cyclic voltammetry (CV) measurements revealed, that currents during polarization with a positive tip bias are extremely low, even at sample temperatures over 300 °C (cf. Fig. 3). At 70 °C, no coherent cyclic voltammetry measurement was possible at all (currents were in the low pA region).

Negative tip biases, in contrast, seem to have a strong effect on the Gd-doped single crystal, which increases with increasing temperature. Oxidation and reduction peaks, which form at 328 °C between biases of -2 V and -3 V are thought to represent the Ce^{3+}/Ce^{4+} redox process (cf. Fig. 3). The noise of the cyclic voltammetry measurements was relatively high, as the contact between AFM tip and sample is not as stable as in a 'standard' measurement setup over longer periods of time.

In Fig. 4, the polarization process during application of -3 V and -5 V is shown at a sample temperature of 254 °C and in dry air. The steady state is already reached at application times of 50 to 75 s. The low signal/noise ratio is on the one hand due to the low currents and on the other hand due to effects of the heating system. From the measurement data, it was calculated, that during a polarization with -5 V for 300 s, a charge of roughly $1.3 \cdot 10^{-5}$ C is applied to the sample.

Positive biases were not investigated, as the currents were extremely low, which was already indicated by cyclic voltammetry (cf. Fig. 3). Fig. 5 illustrates the relaxation of the sample after application of a bias. The sample was polarized for 300 s either in a dry air or N_2 atmosphere. In air, the polarization bias was -5 V, while in N_2, the sample was polarized with -3 V. Generally, the amount of time until a steady state was reached was observed to increase in N_2 atmosphere, but in any case, the effect of the polarization relaxed in less than three minutes. For lower sample temperatures, no coherent measurements were possible anymore, as the currents became too low.

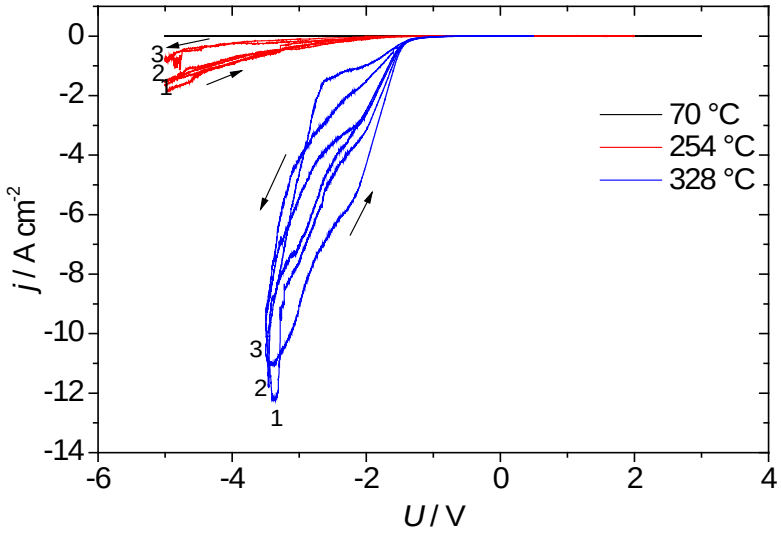

Fig. 3 Cyclic voltammetry measurements at different sample temperatures in dry air. For 70 °C and 254 °C, the scan rate was set at 25 mV/s, for 328 °C the scan rate was set at 50 mV/s. For each measurement, three cycles were performed. Note, that for positive polarization no significant current was observed at any temperature, while for negative polarization increasing current densities were found with increasing temperature.

At room temperature in air, single point measurements with the 5500 AFM setup (using a special current sensing + KPFM nose cone) showed a steady state current of 12.7 ±3 pA (charge of 3.81 ±0.9 nC which is equivalent to charge transport of roughly $2.38 \cdot 10^{10} \pm 5.62 \cdot 10^{9}$ e) for a polarization with -5 V for 300 s. For +5 V for 300 s, the transferred current was below the detection limit of 3 pA (transferred charge < 0.9 nC for the specific measurement time, which equals a charge transfer < $5.62 \cdot 10^{9}$ e). For each bias value, 64 polarization measurements were evaluated. The results are in good accordance to the the CAHT cyclovoltammetry measurements presented in Fig. 3, where the observed currents in the region with positive bias are also near-zero, while for negative bias application an increasing current is visible.

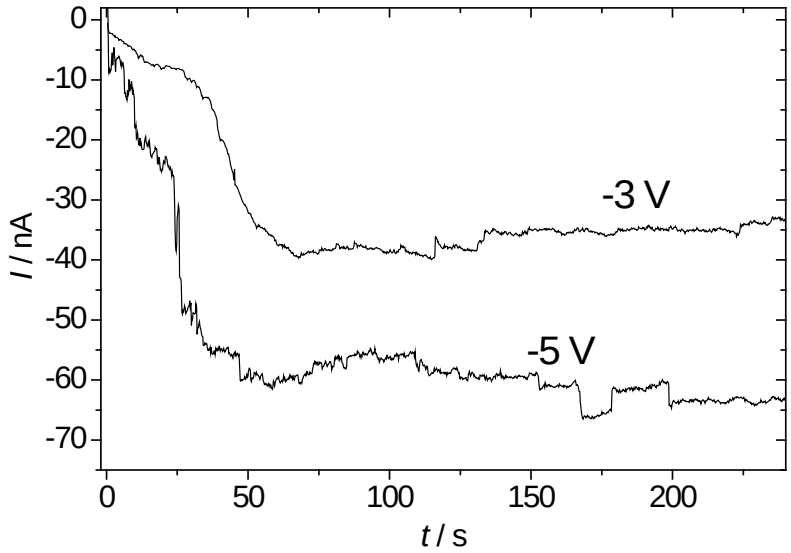

Fig. 4 Polarization measurement with -3 V and -5 V in air at 254 °C. The low signal to noise ratio is due to the small contact diameter between sample and the AFM tip and comparably low contact pressure.

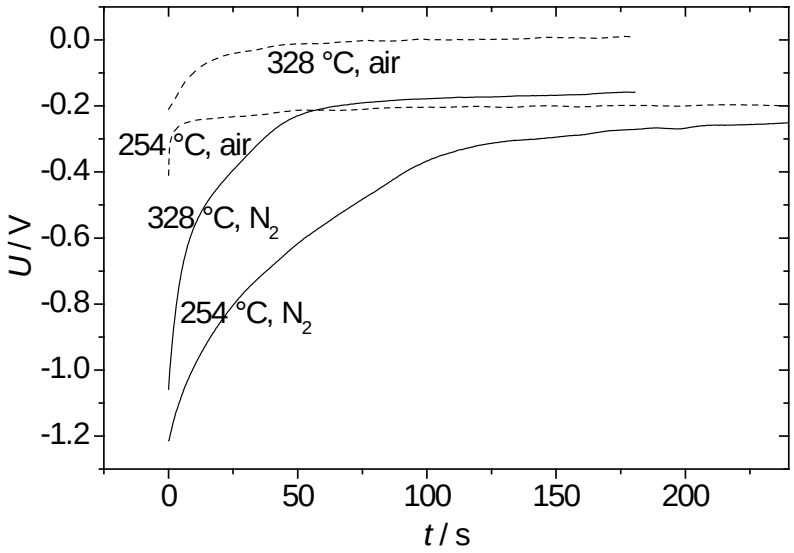

Fig. 5 Relaxation measurement after polarization at two different sample temperatures in dry air or N_2, respectively. Polarization bias was -3 V for 300 s in N_2 and -5 V for 300 s in air. All measurements reach a steady state, but only for 328 °C in air, this steady state was near 0 V. This is due to the effect of the silver paste counter electrode, which can include oxygen to a small extent.

4.2 Effect of negative polarization on the surface potential

Investigations showed that a bias of ±5 V is at least necessary to introduce a detectable surface potential gradient in the material. Subsequently, all measurements were executed with an application of ±5 V for 300 s.

Polarization with -5 V for 300 s led to the development of an area with a decreased surface potential, which was in some cases visible up to 45 minutes after polarization, but normally diminished after 15 minutes (see Fig. 6). The diameter of the affected area was in the range of 3-4 µm in size, the shape was always roughly circular (see blue to yellow area in the upper right image of Fig. 6). After an initial strong increase of the surface potential in the first five minutes, a slower relaxation was observed. At 50 °C, there is already a change of behavior observable for the affected area (cf. Fig. 7). The surface potential distribution does not follow a Gaussian distribution anymore, which was the case at room temperature. Instead, the area with the lowest surface potential occurs in a ring-shape around the area, where the tip was positioned during polarization. The area of the tip-sample contact still shows a decreased surface potential, but it is somewhat higher, than that of the surrounding ‘ring’ (cf. Fig. 7).

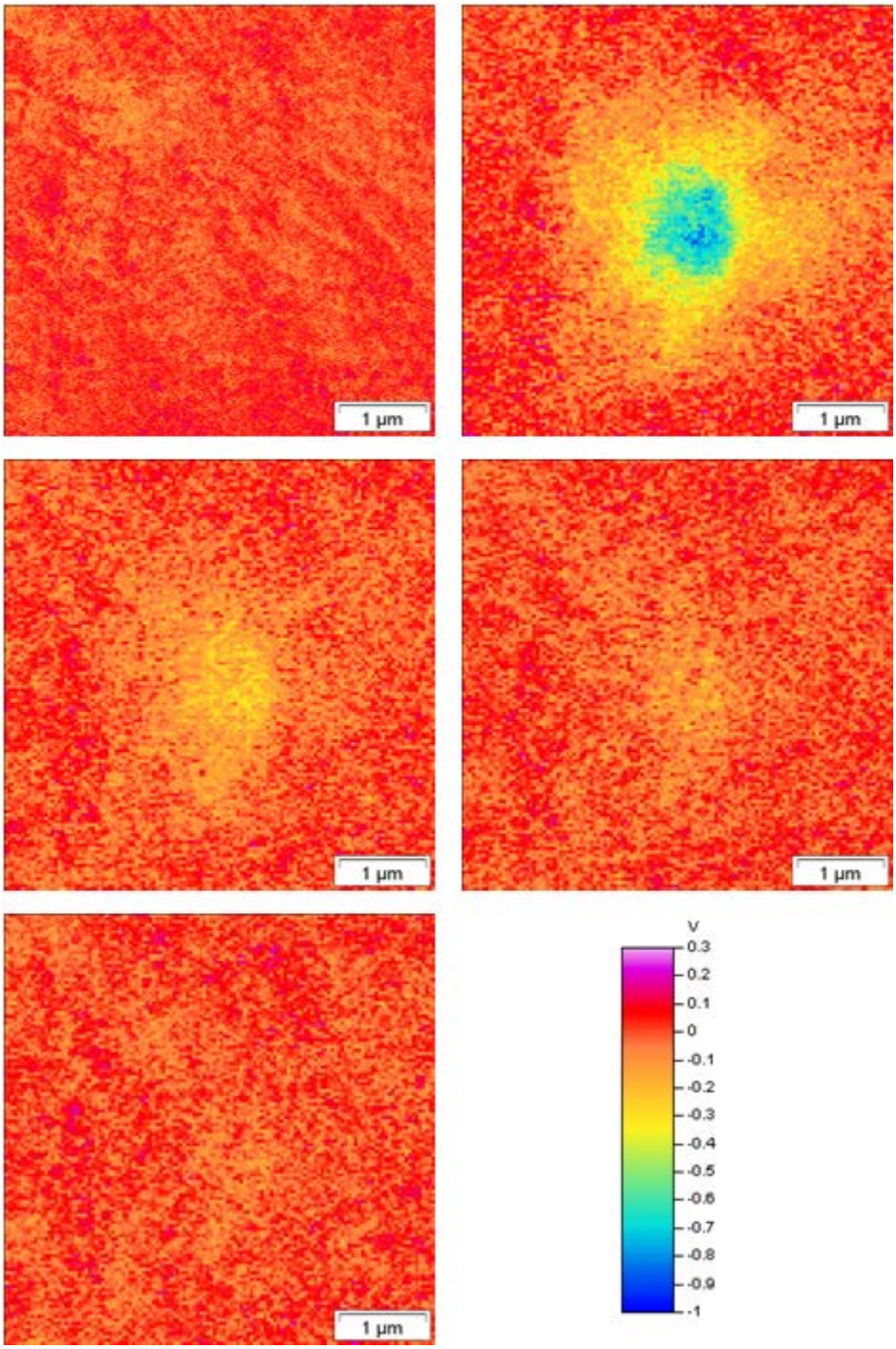

Fig. 6 KPFM images after application of -5 V for 300 s. Top left: KPFM image before the polarization. Top right: 60 s after polarization, middle left: 300 s after end of polarization, middle right: 600 s after polarization. Bottom left: 900 s after polarization.

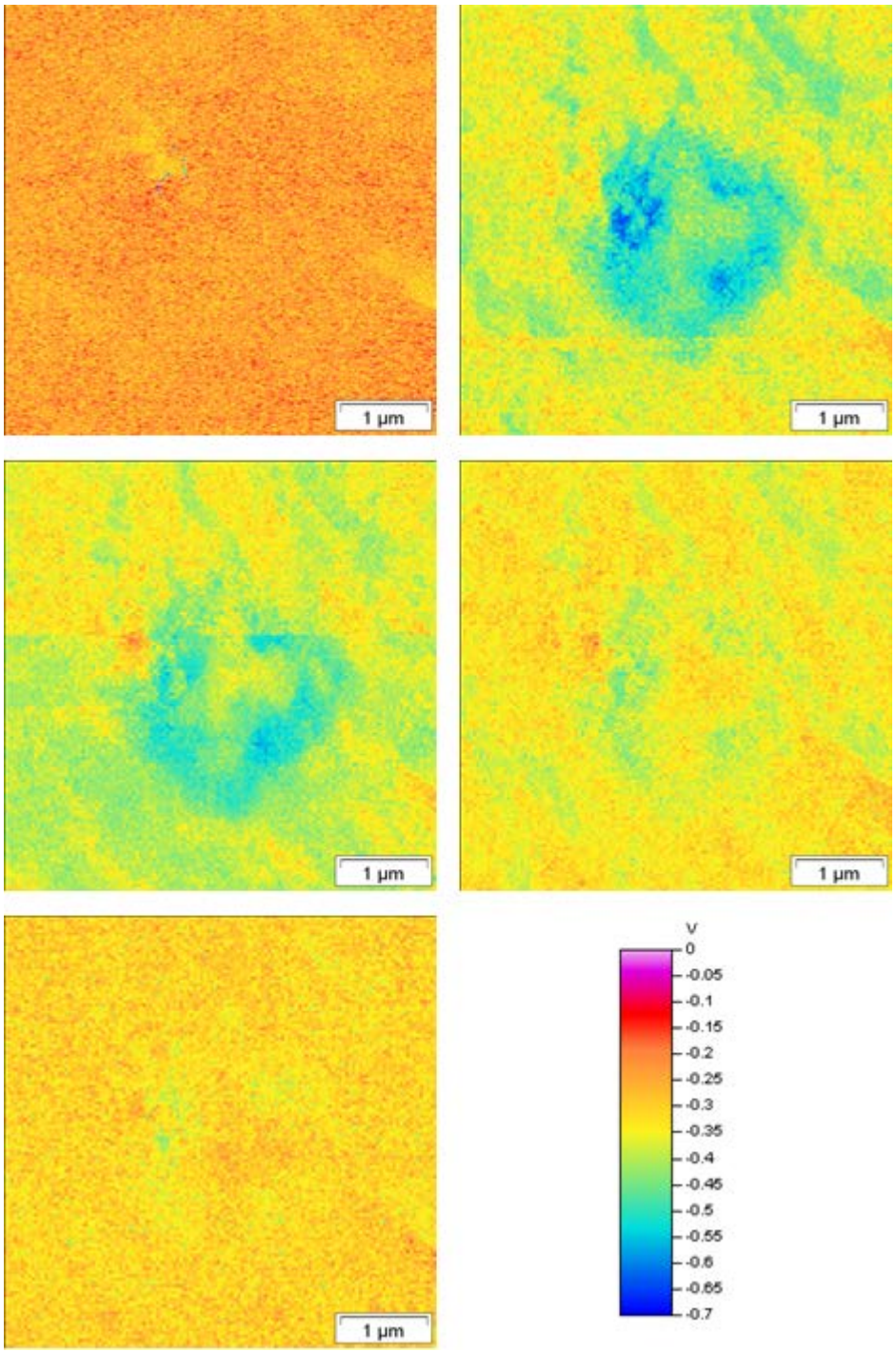

Fig. 7 KPFM images after application of -5 V for 300 s at 50 °C sample temperature in air. Top left: KPFM image before the polarization. Top right: 300 s after polarization, middle left: 600 s after end of polarization, middle right: 1200 s after polarization. Bottom left: 2400 s after polarization.

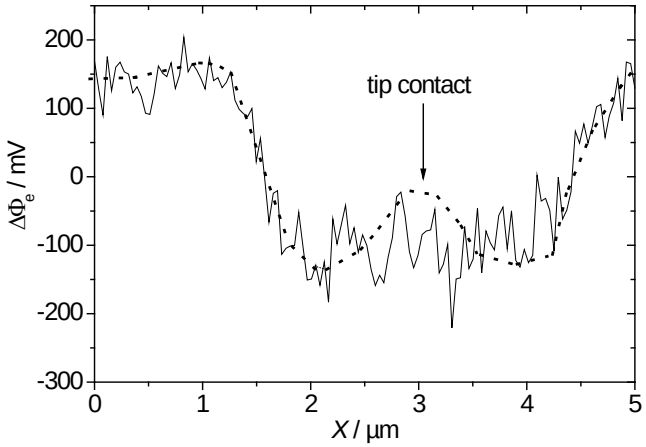

Fig. 8 Measurement values 60 s after the application of -5 V for 300 s at 50 °C. The points indicate the non-Gaussian "ring" shape of the measured curve, which stands in contrast to the Gaussian surface potential distribution which occurs at room temperature. The arrow indicates the area of the tip-sample contact during polarization. Data are not normalized to the pristine potential.

4.3 Effect of positive polarization on the surface potential

After positive polarization with +5 V for 300 s, the contact area around the AFM tip was found to have an increased surface potential (cf. Fig. 9). Compared to negative polarization, though, the effect was significantly less pronounced. $\Delta\Phi_e$ was about 500 to 300 mV after positive charge injection compared to a $\Delta\Phi_e$ of 800 to 600 mV after negative charge injection. Also, the surface potential effect diminished faster and the surface potential signal was in total more diffuse. The affected area was visible in KPFM for up to 30 minutes.

The decay rate of the gradient was already increased at temperatures of 50 °C, although its diameter was decreased (cf. Fig. 9). During the experiments at 50 °C, the effect was visible up to 90 minutes. In contrast to negative polarization, the shape of the gradient was still circular with the minimum at the point, where the tip was positioned during polarization.

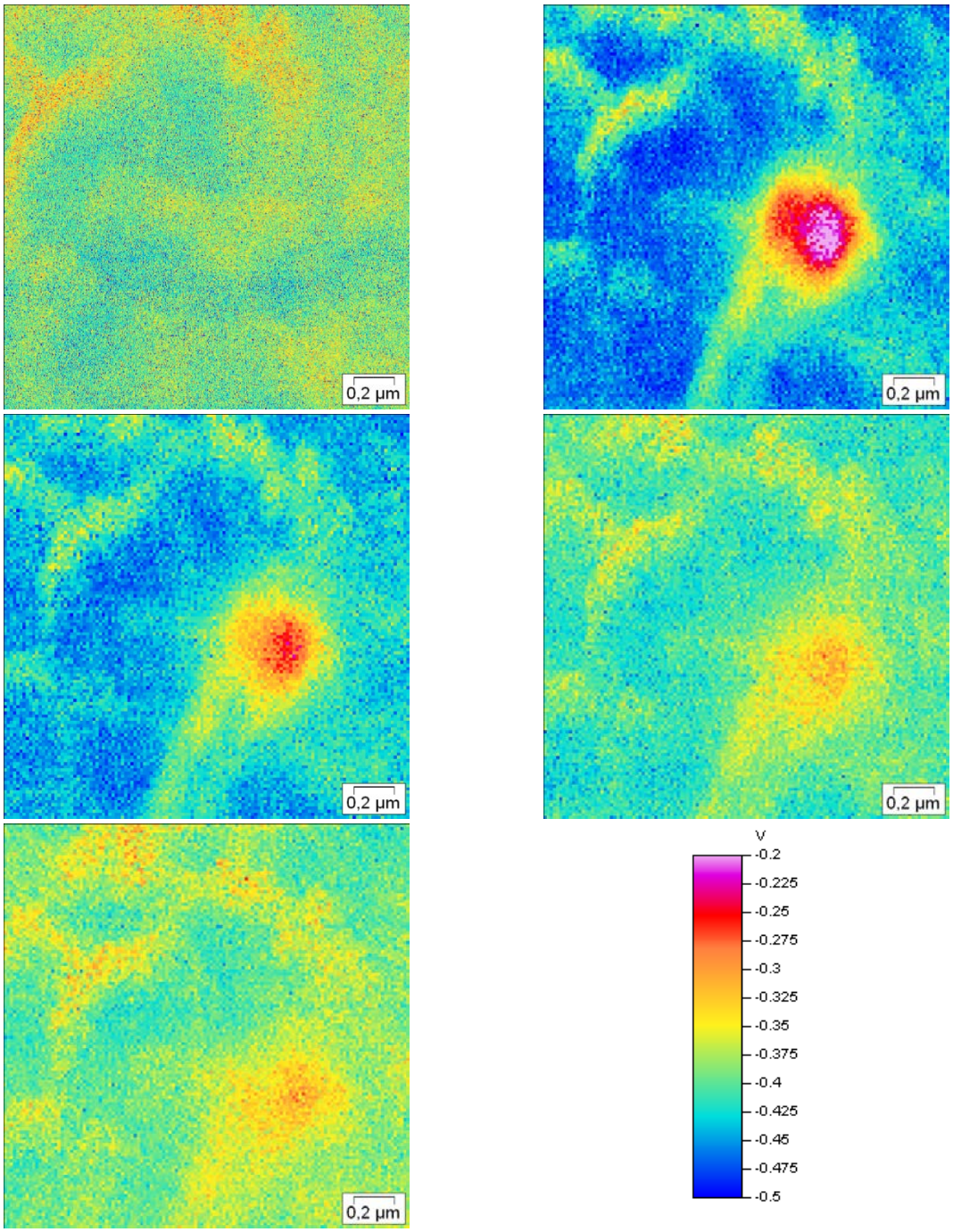

Fig. 9 KPFM images after application of +5 V for 300 s at 50 °C sample temperature in air. Top left: KPFM image before the polarization. Top right: 300 s after polarization, middle left: 600 s after end of polarization, middle right: 1200 s after polarization. Bottom left: 1800 s after polarization.

5 Discussion

For negative polarization, a strong decrease of the surface potential $\Delta\Phi_e$ was observed while positive polarization lead to a significant increase of $\Delta\Phi_e$. These effects can be well explained by the initially mentioned concept of band bending of CGO in contact with the metallic, polarized AFM tip.

By comparing the single point polarization-relaxation measurements with the surface potential measurements after polarization, it can be observed that the KPFM investigations show continuous changes of the sample in a time frame long after steady state is reached for the relaxation measurements. Also, KPFM measurements reveal processes induced by polarization in a temperature range, where standard polarization-relaxation measurements are not possible anymore. From cyclic voltammetry measurements it can also be derived that the charge transport for negative polarization is strongly increased compared to positive polarization due to the redox reaction of $Ce^{3+/4+}$ due to small polaron hopping between Ce^{3+} and Ce^{4+}.

This behavior was also observed for the polarization-KPFM measurements. The differences between the behavior after positive and negative polarization – different relaxation times, different diameter of the affected areas and in case of the measurements at 50 °C even different shapes of the defect gradients - clearly show, that the observed variation is not caused by a simple electron redistribution that takes place on the surface. Instead positive and negative polarization triggers two different redox processes. This is in good accordance to the initial idea, that the local defect mobility is directly influenced by polarization with sufficiently high voltages due to ionization of defect associates. A similar difference for cathodic and anodic polarization has been reported by Farrow et al. during assessment of the local spatial distribution of conductance on CeO_2 thin films [32].

For positive as well as negative biases, the lateral dimension of the gradient stays the same after polarization, although $\Delta\Phi_e$ is converging to the initial state with time. The relaxation process shows an equal decrease of surface potential over time for the whole area (compare Fig. 6, Fig. 7, and Fig. 9). This shows that after the end of polarization, no further lateral transport of defects occurs. This is in good accordance with the initial hypothesis, that a lateral charge transport is only possible as long as a strong electric field is switched on. In fact, the uniform relaxation can only be caused either by a compensation of the local concentration gradient from the bulk material (i.e. recombination of defects to associates to regain electroneutrality) and/or equilibration with the surrounding gas phase (including OH^- molecules from adsorbed water layer).

The variations in intensity of the polarization effect ($\Delta\Phi_e$) were found to mainly depend on the quality of the tip-sample contact during the polarization process. The force on the cantilever was kept constant during all polarization experiments. Still, the AFM tip has a very small diameter and the tip-sample contact can easily be affected by small topographical differences or by the thermal drift from the heating system.

Comparing the diffusion times from the experiments presented here with the diffusion experiments published by Lee et al. [27] for polycrystalline thin films and our own preliminary

results for doped ceria thin films and published data for pellets and Yttria-doped single crystals [31] show that the fading of the effect for our monocrystalline material is rather fast, at least for positive bias application. These findings are in good accordance with the idea, that grain boundaries hinder the defect diffusion in a material due to their Schottky-barrier character [40], but this has to be investigated further. At the same time, this observation can be taken as evidence, that not only the surrounding atmosphere but also the bulk of the material plays a role in the compensation of the introduced defect gradient.

Lee et al. [27] executed measurements in vacuum, where no water layer is observable and still received surface potential gradients after polarization. On the other hand, we can assume that water adsorption on the sample surface is more or less instantaneous when the sample is exposed to humid air. Therefore, the impact of polarization on the water layer would be only measurable for a very short amount of time. Nevertheless, it cannot be ruled out that OH^- uptake in the oxygen vacancies plays a role during the compensation of the surface potential gradient.

Remarkably, it was observed, that a minimum bias of ±5 V was needed for the 10 mol% Gd doped single crystal to produce a large enough $\Delta\Phi_e$ to be detected by KPFM mapping. We assume that the electric field at these voltages is necessary to fully ionize the oxygen defects to sufficiently enhance defect mobility. The bias is much higher than the value reported by Lee et al. [27], who were able to see long-term effects in 20 mol% Gd-doped polycrystalline thin films already after application of ±3 V. Results from measurements with 20 mol% Y-doped single crystals also show effects already at ±3 V [31], while preliminary measurements with single crystals of the composition $Ce_{0.99}Ti_{0.01}O_{2-\delta}$ showed no effects up to ±7.5 V bias application. Also, the $\Delta\Phi_e$ for 20 mol% acceptor doped single crystals was larger for positive as well as negative bias application (Fig. 10). In contrast, the diameter of the affected area 60 s after end of polarization is larger for the CGO10.

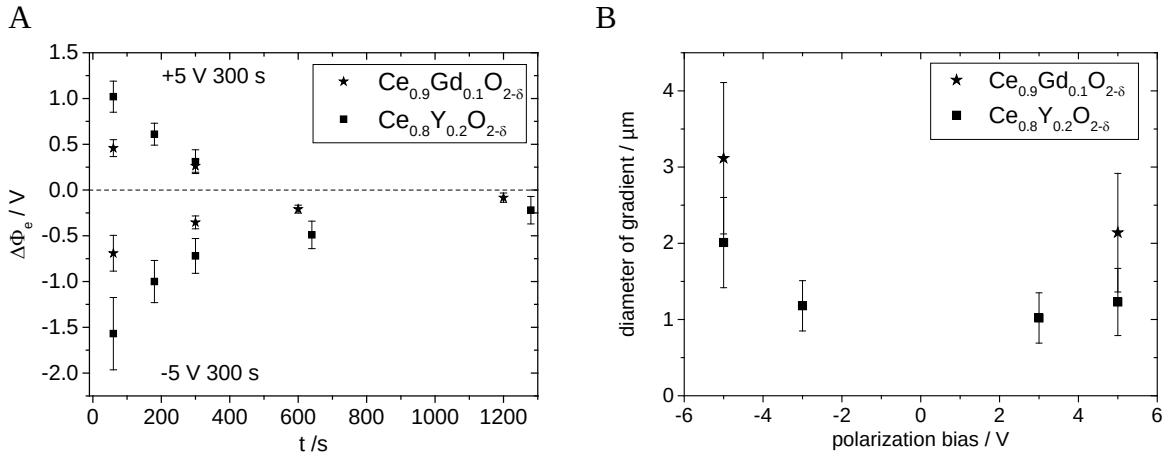

Fig. 10 Comparison of the polarization behavior of 10 mol% Gd-doped and 20 mol% Y-doped single crystals taken from [31]. ΔΦe is referred to the average value in the observation domain before polarization. A) average intensity of the surface potential deviation and decay behavior after the end of the polarization and relaxation of the maximum/minimum ΔΦe with time, B) average lateral diameter of the gradient 60 s after end of polarization.

We predict in a first instance that a higher concentration of oxygen vacancies, which is thought to be equal to the acceptor dopant concentration, facilitates the change of defect concentration

by polarization at low temperature. As explanation for the different diameters, we assume that the depth of penetration of the polarization effect becomes larger for increased acceptor dopant concentrations. For low acceptor dopant concentrations, in contrast, more of the charge is transported directly in the uppermost surface layers, leading to a larger diameter of the effect for 10 mol% compared to 20 mol% acceptor doped material.

Altogether, we assume the ionization of defect associates to be the most plausible hypothesis to describe the processes during and after polarization. It can be assumed that positive polarization ionizes defects and leads to the local oxidation of Ce^{3+} to Ce^{4+}. Negative polarization can cause a mobilization of partially ionized defects by allocation of higher Ce^{3+} concentrations. A local oxidation of cerium ions as well as higher concentrations of $V_O^{\circ\circ}$ are assumed to lead to a higher surface potential while a local reduction of cerium ions as well as transport of V_O° or V_O can be imagined to locally lower the surface potential in addition to the initially mentioned band bending. The observed differences in diameter and intensity of the affected regions can be explained by different activation energies for the respective redox processes and by different mobilities of the generated defect species.

6 Conclusion

The presented measurement show that KPFM is a versatile tool for measuring and understanding complex electrochemical surface processes at low temperatures, where standard measurement techniques failed due to the very low conductivity of $Ce_{0.9}Gd_{0.1}O_{2-\delta}$. Further, due to the very good lateral resolution, it is possible to probe chosen points of a sample. For future investigations, this rises the opportunity to probe grains and grain boundaries in polycrystalline samples independently.

7 Acknowledgements

The authors want to acknowledge the German Research Society (DFG) for funding within the collaborative project "CeO_2 based oxides as redox active materials for exchange and storage of oxygen" (grant no. WI952/9-1 and LE781/14-1). This work was supported financially by The Programme Commission on Sustainable Energy and Environment, The Danish Council for Strategic Research, via the Strategic Electro-chemistry Research Center (SERC) (www.serc.dk), Contract No. 2104-06-0011, and by The Catalysis for Sustainable Energy (CASE) initiative funded by the Danish Ministry of Science, Technology, and Innovation.

8 Literature

[1] H. Inaba, H. Tagawa, *Solid State Ionics* **83** (1996) (1-2) 1.
[2] V.V. Kharton, F.M. Figueiredo, L. Navarro, E.N. Naumovich, A.V. Kovalevsky, A.A. Yaremchenko, A.P. Viskup, A. Carneiro, F.M.B. Marques, J.R. Frade, *J Mater Sci* **36** (2001) 1105.
[3] M. Mogensen, N.M. Sammes, G.A. Tompsett, *Solid State Ionics* **129** (2000) 63.
[4] T.S. Stefanik, H.L. Tuller, *J Eur Ceram Soc* **21** (2001) (10–11) 1967.
[5] B.C.H. Steele, *Solid State Ionics* **129** (2000) (1-4) 95.

[6] N. Mahato, A. Gupta, K. Balani, *Nanomaterials and Energy* **1** (2011) (1) 27.
[7] L. Vivier, D. Duprez, *Chem Sus Chem* **3** (2010) (6) 654.
[8] E. Aneggi, M. Boaro, C. de Leitenburg, G. Dolcetti, A. Trovarelli, *J Alloy Comp* **408–412** (2006) (0) 1096.
[9] N.J. Lawrence, J.R. Brewer, L. Wang, T.-S. Wu, J. Wells-Kingsbury, M.M. Ihrig, G. Wang, Y.-L. Soo, W.-N. Mei, C.L. Cheung, *Nano Letters* **11** (2011) (7) 2666.
[10] M. Huang, S. Fabris, *Phys. Rev. B* **75** (2007) (8) 081404.
[11] J. Zhang, H. Kumagai, K. Yamamura, S. Ohara, S. Takami, A. Morikawa, H. Shinjoh, K. Kaneko, T. Adschiri, A. Suda, *Nano Letters* **11** (2011) (2) 361.
[12] K. Schmale, M. Grünebaum, M. Janssen, S. Baumann, F. Schulze-Küppers, H.-D. Wiemhöfer, *Phys Stat Sol B* **248** (2011) (2) 314.
[13] S. Lübke, H.-D. Wiemhöfer, *Solid State Ionics* **117** (1999) (3–4) 229.
[14] Y. Namai, K.-I. Fukui, Y. Iwasawa, *Catal Today* **85** (2003) (2–4) 79.
[15] K. Sasaki, J. Maier, *J Appl Phys* **86** (1999) (10) 5422.
[16] K. Sasaki, J. Maier, *J Appl Phys* **86** (1999) (10) 5434.
[17] F. Esch, S. Fabris, L. Zhou, T. Montini, C. Africh, P. Fornasiero, G. Comelli, R. Rosei, *Science* **309** (2005) (5735) 752.
[18] C.T. Campbell, C.H.F. Peden, *Science* **309** (2005) (5735) 713.
[19] H.L. Tuller, A.S. Nowick, *J Electrochem Soc* **122** (1975) (2) 255.
[20] M. Nonnenmacher, M.P. O'Boyle, H.K. Wickramasinghe, *Appl Phys Lett* **58** (1991) (25) 2921.
[21] M. Nonnenmacher, M. O'Boyle, H.K. Wickramasinghe, *Ultramicroscopy* **42-44** (1992) (Part 1) 268.
[22] W. Melitz, J. Shen, A.C. Kummel, S. Lee, *Surf Sci Rep* **66** (2011) (1) 1.
[23] T. Mélin, M. Zdrojek, D. Brunel, In: B. Bhushan, Editor, *Scanning Probe Microscopy in Nanoscience and Nanotechnology*, Springer, Berlin (2010), p.89-128.
[24] U. Zerweck, C. Loppacher, T. Otto, S. Grafström, L.M. Eng, *Phys Rev B* **71** (2005) (12) 125424.
[25] H.O. Jacobs, P. Leuchtmann, O.J. Homan, A. Stemmer, *J Appl Phys* **84** (1998) (3) 1168.
[26] K. Schmale, J. Barthel, M. Bernemann, M. Grünebaum, S. Koops, M. Schmidt, J. Mayer, H.D. Wiemhöfer, *J Sol State Electrochem* **17** (2013) (11) 2897.
[27] W. Lee, M. Lee, Y.-B. Kim, F.B. Prinz, *Nanotechnology* **20** (2009) (44) 445706.
[28] Z. Zhang, J.T. Yates, *Chem Rev* **112** (2012) (10) 5520.
[29] K. Sasaki, J. Claus, J. Maier, *Solid State Ionics* **121** (1999) 51
[30] J. Maier, *Phys Chem Chem Phys* **5** (2003) (11) 2164.
[31] K. Neuhaus, F. Schulze-Küppers, S. Baumann, G. Ulbrich, M. Lerch, H.-D. Wiemhöfer, *Solid State Ionics* **288** (2016) 325.
[32] T. Farrow, N. Yang, S. Doria, A. Belianinov, S. Jesse, T.M. Arruda, G. Balestrino, S.V. Kalinin, A. Kumar, *APL Mater* **3** (2015) (3) 036106.
[33] N. Yang, S. Doria, A. Kumar, J.H. Jang, T.M. Arruda, A. Tebano, S. Jesse, I.N. Ivanov, A.P. Baddorf, E. Strelcov, S. Licoccia, A.Y. Borisevich, G. Balestrino, S.V. Kalinin, *Nanotechnology* **25** (2014) (7) 075701.
[34] S. Kim, U. Anselmi-Tamburini, H.J. Park, M. Martin, Z.A. Munir, *Adv Mater* **20** (2008) (3) 556.
[35] H.J. Avila-Paredes, C.-T. Chen, S. Wang, R.A. De Souza, M. Martin, Z. Munira, S. Kim, *J Mater Chem* **20** (2010) 10110.
[36] K.V. Hansen, Y. Wu, T. Jacobsen, M.B. Mogensen, L. Theil Kuhn, *Rev Sci Inst* **84** (2013) (7) 073701.
[37] A. Kumar, T.M. Arruda, Y. Kim, I.N. Ivanov, S. Jesse, C.W. Bark, N.C. Bristowe, E. Artacho, P.B. Littlewood, C.-B. Eom, S.V. Kalinin, *ACS Nano* **6** (2012) (5) 3841.
[38] H.R. Harrison, J.M. Honig, *Bull Mater Sci* **3** (1981) (3) 247.

[39] W. Assmus, N. Whippey, *Chem Ing Tech* **55** (1983) (9) 716.
[40] R. Waser, R. Hagenbeck, *Acta Materialia* **48** (2000) (4) 797.